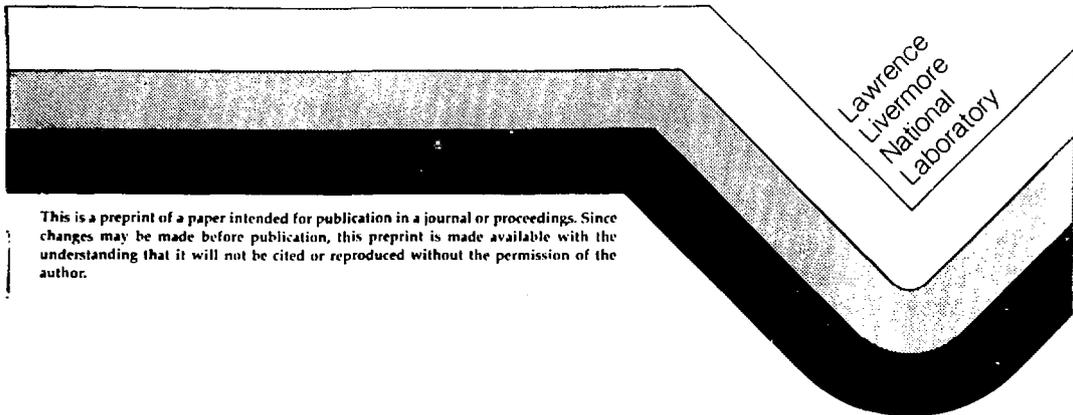# HIGH CURRENT DENSITY MAGNETS FOR INTOR AND TIBER

J. R. MILLER
C. D. HENNING
J. A. KERNS
D. S. SLACK
L. T. SUMMERS
J. P. ZBASNIK

Lawrence
Livermore
National
Laboratory

DISCLAIMER

HIGH CURRENT DENSITY MAGNETS FOR INTOR AND TIBER*

J. R. Miller, C. D. Henning, J. A. Kerns, D. S. Slack,
L. T. Summers, and J. P. Zbasnik

INTRODUCTION

The adoption of high current density, high field, superconducting magnets for INTOR and TIBER would prove beneficial. When combined with improved radiation tolerance of the magnets to minimize the inner leg shielding, a substantial reduction in machine dimensions and capital costs can be achieved. Fortunately, cable-in-conduit conductors (CICC) which are capable of the desired enhancements are being developed. Because conductor stability in a CICC depends more on the trapped helium enthalpy, rather than the copper resistivity, higher current densities of the order of 40 A/mm^2 at 12 T are possible. Radiation damage to the copper stabilizer is less important because the growth in resistance is a second-order effect on stability. Such CICC conductors lend themselves naturally to niobium-tin utilization, with the benefits of the high current-sharing temperature of this material being taken to advantage in absorbing radiation heating. When the helium coolant is injected at near the critical pressure, Joule-Thompson expansion in the flow path tends to stabilize the fluid temperature at under 6 K. Thus, higher fields, as well as higher current densities, can be considered for INTOR or TIBER.

Peak nuclear heating rates above 5 mW/cm^3 are cryogenically acceptable with large refrigerators. This corresponds to a neutron damage of 10^{19} n/cm^2 or insulator damage levels of 10^{10} rads in about 10^8 seconds. These values are compatible with next generation engineering test reactors, so long as polyimide insulators provide the main voltage standoffs.

PERSPECTIVE

Our experience with superconducting magnets built with CICCs is **MASTER** relatively recent, but the experience has been good and the promise is

better still. Actual coil operating experience has been bolstered
tremendously by small scale test and development activities at a number of
laboratories in the US, Japan, and Europe. Figure 1 gives some perspective
of what has been achieved with CICC windings and the goals of present
development activities, represented in terms of operating current density
over the cable space, (i.e., inside the conduit of the CICC) vs maximum
field at the windings. Curve 1 shows what can reasonably be expected with
NbTi windings if a stability margin against an external pertubation of 100
mJ/cm^3 of conductor is needed. This curve has been bracketed by the
performance of a small solenoid built and tested extensively at ORNL.[1] The
lower, solid square represents operation where the measured stability margin
was well in excess of 100 mJ/cm^3. The solenoid operated quite stably up to
the critical current, but at the point represented by the open square the
stability margin was measured to be 56 mJ/cm^3.

The Δ, the ▼, and the ▽ represent performance of coils wound with
nearly identical CICCs using multifilamentary (MF-)Nb_3Sn. The first is the
planned operating point of the Westinghouse LCT coil and the latter two,
the demonstrated performance of the MIT 12 T coil, which was tested in the
LLNL, High Field Test Facility (HFTF).[3] The lower of the two MIT 12 T
points represents the only point where stability of the coil was tested.
The coil stably absorbed a pulse of >200 mJ/cm^3 without consequence, but the
heater for stability testing was destroyed.

Curve 2 is a projection of the performance that is obtainable with
state-of-art MF-Nb_3Sn in a CICC design. The projected improvement is
dramatic and is possible because the performance of a CICC is tied directly
to the increased current margin (or alternatively, increased temperature
margin) provided by recent improvements in the critical currents of MF-Nb_3Sn
wires. The ● shows that the design for the high field grade of the TIBER II
pusher coil, while aggressive, is well within the obtainable performance.

Curve 3 takes account of the effects of radiation damage to the copper
stabilizer in transforming the estimated performance boundary of Curve 2 to
one appropriate to the expectations for the TIBER II TF coil environment,
where shielding is much reduced. The design point o for the TF coils falls

-2-

within the obtainable performance region. Some simplications were necessarily made in generating Curves 1-3. However, we will now summarize in some detail the design considerations for conductors for TIBER II as specific examples, and thereby give credibility to the curves of Fig. 1.

Requirements for TIBER II--The TIBER II design emphasizes compactness as a means to machine economy. High performance in the superconducting coil systems is essential to the achievement of compactness. The high performance goals for the magnet systems of TIBER II are exemplified by the requirements placed on the TF coils and the central, plasma-shaping or "pusher" coil. These coils are highlighted in the schematic of the TIBER II magnet system in Fig. 2.

For the present, we consider only steady field operation, as would be the case for TIBER II with an rf-driven plasma current. The pusher coil requirement can then be simply stated as a total current requirement of 18 MA, which can be achieved with a coil 1.1-m i.d. x 1.9-m o.d. x 1.13-m height, having an average winding pack current density of 40 A/mm^2. The resulting maximum field for this coil is 14 T. The TF system must produce 6 T at the plasma major radius of 3 m. When space for the plasma, blanket, shield, etc. is considered, one finds that a TF coil must have an opening about 6 m on the vertical x 4 m on the horizontal. These and other electromagnetic requirements can be met with a 16 coil set. Because of space requirements the winding pack must have an average current density of 40 A/mm^2 and will see a maximum field of 12 T.

The large plasma shaping and TF coil systems must have high conductor stability but the designs will be driven as much by protection requirements vis-a-vis high current density and high stored energy as they will by stability requirements. The design of the TF system, because of its nearness to the plasma and because of reduced shielding (also for compactness and reduced costs), must also account for the effects of nuclear heating in the superconductor approaching 10 mW/cm^3 in places, neutron fluence at the superconductor on the order of 10^{19} n/cm^2, damage to the copper stabilizer on the order of 0.02 dpa at end-of-life, and radiation

exposure to insulating materials in the winding pack of the order of 10^{10} rad.

CONDUCTOR PERFORMANCE

Available performance in superconductor wire--Figure 3 is a compilation by Suenaga[4] of critical current data for several MF-Nb_3Sn conductors at 4.2 K. The solid curves represent variants of Nb_3Sn with Ti additions, i.e. $(NbTi)_3Sn$; the particular data base used for the TIBER I study[5] is the heavier curve. The broken curves represent variants of "pure" or unmodified Nb_3Sn. Note that generally the $(NbTi)_3Sn$ conductors perform better at the higher fields. This is because both T_{c0} and B_{c20} have been improved by the Ti additions. At 12 T and below, Nb_3Sn performs essentially as well as the $(NbTi)_3Sn$, or even better in some instances. At these lower fields, the obtainable critical current density is dominated by microstructure and its effect on the density of flux pinning sites in the superconductor. For a number of reasons, the microstructure of Nb_3Sn is presently being better controlled in the manufacturing processes.

Radiation damage limits in superconductors--The data of Fig. 4 are generally representative of the effects of high energy neutron fluence on technical Nb_3Sn conductors, pure and modified.[6] The samples tested were irradiated with 14.1 MeV neutrons at room temperature, then tested at 4.2 K. The lower horizontal axis in Fig. 4 accounts for the "softer" neutron energy-spectrum expected in TIBER II. The initial increases in performance apparent in these data are explained in terms of the damage giving rise to increased normal state resistivity of the superconductors. An increase in the normal state resistivity can result in an increase in the upper critical field. In the modified materials the upper critical field has already been optimized by additions of a third element to increase the normal state resistivity. Therefore, any further increase due to damage might be expected to be small. Eventually, the decrease in performance is caused by a drop in T_c with increased damage. For unmodified Nb_3Sn, it is clear that the conductor will retain its performance beyond 10^{19} n/cm^2 fluence in TIBER II. Modified Nb_3Sn will be useful for attaining the required performance in

the pusher coil where the high field windings are essentially completely
shielded by the TF system and the outer, lower field turns.

Radiation damage in stabilizer—Stability in a CICC is obtained
primarily from the enthalpy available in the internal helium over the
temperature margin provided by operating the conductor at less than its
critical current. As a result, there is not a big penalty on stability as
the conductivity of the copper is reduced by accumulated damage. Only
copper is considered as a stabilizer. The damage to high purity aluminum at
the fluences under consideration give rise to end-of-life conductivities as
bad or worse than copper. Manufacturing difficulties and other less
desirable properties then eliminate it from consideration. However, we will
certainly want to protect the TIBER II magnets against damage in the event
of a quench, right up to the end of life of the machine. Knowledge of
copper resistivity vs damage is essential for providing the needed
protection. For our conceptual designs we assume the initial residual
resistivity $\rho_{o,i}$ of the copper to be increased by radiation damage during
operation by

$$\rho_d = \rho_s[1 - \exp(-iD/\rho_s)],$$

where $\rho_s = 3.46$ n$\Omega \cdot$m is the saturation level and $i = 696$ n$\Omega \cdot$m$\cdot$dpa^{-1} is the
saturation rate. It is expected that normal operation will be interrupted
at intervals, and room temperature anneal cycles will be possible. These
anneals may be accounted in computing the end-of-life resistivity increase
from a relation of the form

$$\rho_o = \rho_d \left(\sum_{n=0}^{N} f_{ret}^n\right) + \rho_{o,i}$$

where N is the number of regular anneals, and f_{ret} is the fraction of damage
resistivity retained after an anneal cycle, and depends on the damage
approximately as $f_{ret} = 0.01 + 0.2\exp(-iD/\rho_s)$. Magnetoresistivity is accounted
for by the relation

$$\rho_{cu}(B) = \rho_o[1 + 0.0339(B/\rho_o)^{1.07}],$$

(resistivity in $n\Omega \cdot m$) where ρ_0 includes the effects of radiation damage.[7]

Strain effects in superconductors--In a CICC system, the strain in the Nb_3Sn filaments, and thus the critical current at operating conditions, is determined by the complex interaction of the sheath and the cable inside during the entire history from formation at around 1000 K, through cooldown to the operating temperature around 4 K, to charging to full field and current resulting in high electromagnetic forces borne principally by the sheath. An experimental program is underway at LLNL to examine the conductor/sheath interaction through a series of electromechanical tests. Some results are already available.[8]

In the first series of tests, the critical currents of model CICC's were measured, with the axial load applied to the sheath during each test increased by small increments until the measured critical current was observed to pass through a maximum. The ratio I_{ci}/I_{cm} of initial or "no load" critical current to maximum critical current was observed to vary withfraction of the internal space available for He in the otherwise identical specimens.[8] These data are plotted in Fig. 5, along with other values for similar conductors inferred from data in the literature.[9],[10]

To a first approximation, I_{ci}/I_{cm} gives a measure of superconductor filament strain in the unloaded state of the CICC. For a single wire (of the same manufacture as all those represented in Fig. 5 and tested under the same conditions of temperature and field), Ekin give I_c/I_{cm} vs filament strain as in Fig. 6.[11] But also, initial axial strain in the filaments following cooldown should be related to the thermomechanical properties of the various constituents of the CICC according to a relation of the form:[8]

$$\epsilon_{init.} = \frac{F(f_{He})E_{sh}A_{sh}[(\frac{\Delta \ell}{\ell})_{sh} - (\frac{\Delta \ell}{\ell})_{fil}] - (\sigma_{Cu,y}A_{Cu} + \sigma_{bz,y}A_{bz})}{F(f_{He})E_{sh}A_{sh} + E_{fil}A_{fil}} , \quad (1)$$

A factor $F(f_{He})$ has been introduced before the sheath modulus to account for the observation that the greater the He fraction the less rigidly linked are the conductor strands to the compressive influence of the sheath during cooldown.

We may use the formalism represented in Fig. 6 to convert the data of Fig. 5 to ε_{init} vs f_{He}. These data can in turn be converted to a representation of $F(f_{He})$ vs f_{He} as shown in Fig. 7, using Eq. (1).[8] We expect this conversion process to hold for conductors of reasonably similar geometry. The curve $F(f_{He}) = 0.15 \exp [-(f_{He}/0.4)^2]$ gives a reasonable fit to the best verified data.

The sheath of a CICC is the principal load bearing member. We expect the tensile strain in the filaments at operating conditions to be given by an expression of the form

$$\varepsilon = \varepsilon_{init.} + C \, \varepsilon_{sh} \tag{2}$$

with the first term determined from Eq. (1) and the fit to data in Fig. 7. The factor C in Eq. (2) is presently under experimental investigation in the LLNL high field coil development program, but we expect it to be nearly constant and of order unity.

In the range of temperatures over which superconductors are usually operated, critical current density is essentially a linear function of temperature and can be accurately represented at a particular field B and strain ε by the extrapolated intercepts $J_{c0}(B,\varepsilon)$ and $T_c(B,\varepsilon)$. According to Ekin,[11] these have the functional forms

$$J_{c0}(B,\varepsilon) = J_{c0m}(B)\left(1 - a|\varepsilon|^{1.7}\right)^{1/2}$$

$$x \quad \frac{\left[1 - \dfrac{B}{B_{c2m}(0)\left(1 - a|\varepsilon|^{1.7}\right)}\right]^2}{\left[1 - \dfrac{B}{B_{c2m}(0)}\right]^2} \quad ,$$

$$T_c(B,\varepsilon) = T_{cm}(B)\left(1 - a|\varepsilon|^{1.7}\right)^{1/3}$$

$$x \quad \frac{\left[1 - \dfrac{B}{B_{c2m}(0)\left(1 - a|\varepsilon|^{1.7}\right)}\right]^{1/2}}{\left[1 - \dfrac{B}{B_{c2m}(0)}\right]^{1/2}} \quad ,$$

$$a = 900 \text{ for } \epsilon \leq 0 ,$$
$$a = 1250 \text{ for } \epsilon > 0 .$$

Conductor Stability--The critical values above enter the relation for the stability parameter η according to

$$\eta = \frac{\left(1 - f_{cond}\right)}{f_{cond}} \left\{ \frac{[T_c(B,\epsilon) - T_b]}{T_c(B,\epsilon)} - \frac{J}{f_{cond}(1 - f_{Cu}) J_{c0}(B,\epsilon)} \right\} .$$

The stability parameter is merely a dimensionless parameter constructed so as to vary monotonically with the actual stability margin of a CICC so long as the interstitial helium is fully utilized to absorb the energy of a perturbation.[12]

With superconductor performance defined by the critical parameters J_{c0} and T_c, the stability of a CICC operating with cable space current density J and at field B and temperature T_b is then essentially determined by the fraction of conductor f_{cond} filling the cable space and the fraction of copper f_{Cu} in the conductor strands. Figure 8 shows typical contours of the stability parameter mapped in the (f_{cond}, f_{cu}) plane at particular values of J, B and T_b. For this discussion the values are not important, only the forms of the contours. The solid curves take account of conductor strain effects as discussed above and the dashed curves ignore these effects. The conceptional analyses presented here include strain effects as described above with $F(f_{He})$ given by the fitted curve in Fig. 7 and with $C = 0.86$ in Eq. (2).

It must be borne in mind that the contours of Fig. 8 give a measure of stability available from the CICC only if all the interstitial helium in the vicinity of a disturbance is fully utilized. Full utilization, of course, depends upon heat transfer from the strands of the cable to the bulk of the fluid. With adequate flow, i.e. flow sufficient to cause turbulence, the heat transfer is good. Even with initially stagnant helium, however, the transient flow caused by the disturbance can be enough to generate the necessary turbulence. Whether the transient flow is sufficient depends on the cable space current density J and various conductor parameters.[12] The following phenomenologically derived and empirically verified relation

-8-

places a constraint upon J such that heat transfer is adequate to ensure that the heat capacity of the internal helium is fully utilized:[12]

$$J \leq \left[\frac{f_{Cu} \, f^3_{cond}}{(1-f_{cond})} \right]^{1/2} \frac{[T_c(B,\epsilon) - T_b]^{1/2} \, \ell_H^{2/15}}{\rho_{Cu}^{1/2} \, \tau_H^{1/15} \, d_w} \tag{3}$$

Since (3) is relatively insensitive to ℓ_H and τ_H, we usually assume $\tau_H = 1$ ms and $\ell_H = 10$ m unless specific situations suggest different values.

When this relation is satisfied the stability margin available can be estimated from an empirically based relationship of the form:

$$e_p = \frac{n \, S_{He} \, T_c}{\left(1 + \dfrac{J^2 \, \rho_{Cu} \, C \, d_w}{f_{cu} \, f^2_{cond}} \right)} \tag{4}$$

In this relation S_{He} is the mean volumetric heat capacity of the interstitial helium in the operating range. We generally estimate S_{He} by evaluating

$$S_{He} = \frac{\int_{T_b}^{T_{cs}} \rho_{He} \, C_p \, dT}{\left(T_{cs} - T_b \right)} \quad ,$$

with constant pressure values used for the integrand. Depending on conditions, S_{He} may have surprisingly simple form, as shown in Fig. 9, which corresponds to $T_b = 4.5$ K, $p = 6$ atm.[13] The second term in the denominator of (4) is an approximate accounting for Joule heat production during the recovery process. When (3) is satisfied, recovery is rapid and the term is small (~10-20% of e_p). Experimental data are consistent with the recovery time being represented as $\tau_R = C \, e_p \, d_w$ with $C \approx 50 \times 10^{-6}$ $W^{-1} \cdot m^{-1}$.

Protection--The current density in the cable space of a CICC must be constrained to be compatible with protection requirements; i.e. in the event of a quench, the temperature at any point must not rise above some safe value and the pressure inside the conduit must not exceed some safe value.

-9-

What is a safe temperature may be defined by the "hot spot" temperature in relation to temperatures elsewhere in the coil since thermal stresses caused by high temperature gradients could be sufficient to cause damage. What is a safe maximum pressure will be determined by the shape and thickness of the conduit walls.

The cable space current density is constrained by maximum hot spot temperature according to a relation of the form:[12]

$$
J \leq \left\{ \frac{V_D I_{op}}{E_s} \left[(1 - f_{cond}) \, f_{cond} \, f_{Cu} \, I_1 \right. \right.
$$
$$
+ \, f_{Cu}^2 \, f_{cond}^2 \, I_2
$$
$$
\left. \left. + \, (1 - f_{Cu}) \, f_{Cu} \, f_{cond}^2 \, I_3 \right] \right\}^{1/2} ,
$$

where   (5)

$$
I_1 = \int_{T_b}^{T_{max}} \frac{\mu_{He,init.} C_{v,He}}{\rho_{Cu}} \, dT ,
$$

$$
I_2 = \int_{T_b}^{T_{max}} \frac{\mu_{Cu} C_{Cu}}{\rho_{Cu}} \, dT ,
$$

$$
I_3 = \int_{T_b}^{T_{max}} \frac{\mu_{Core} C_{Core}}{\rho_{Cu}} \, dT .
$$

The above is seen to be conservative when compared with experiment (the observed temperature rise is lower), as might be expected since it ignores the roles of the steel sheath and any insulating materials as heat absorbents. For short times this is good practice because of the poor thermal diffusivity of these materials, but for longer times they can be expected to absorb appreciable heat.

The maximum allowable pressure in the event of a quench constrains J according to[12]

$$J \leq \frac{6.59 \ p_{max}^{0.694} \ f_{Cu}^{1/2} \ f_{cond}^{1/4} \ (1-f_{cond})^{3/4} \ d_w^{1/4}}{L^{3/4} \ \rho_{Cu}^{1/2}} . \tag{6}$$

We view this as a worst case. It corresponds to an entire flow path quenched instantaneously and held normal until the helium has vented. However, recent calculations indicate that other cases may result in pressures of the same order depending on detection time.[14] This criterion may be relaxed in designs where assurance can be had that it is unrealistic. We are working to provide experimental validation of the proper quench pressure criterion.

As can be seen from the above, the constraints on J are dependent upon choices of conductor fraction inside the conduit and copper fraction inside the conductor. Figure 10 shows the strain dependent contours of η from the example of Fig. 8 with contours where the constraints on J addressed above are just met in a particular design. Allowed values of (f_{cond}, f_{Cu}) are generally above these contours. At the specified current density, we choose conductor designs that give the highest stability parameter allowed by the constraints. If the stability is more than adequate, a higher J can be chosen and the optimization repeated.

Radiation heating--The direct heating in the windings of a coil caused by absorbed radiation must be removed by forced flow of the internal helium in the CICC. Highest heat capacity of the fluid over the temperature range of interest is available at pressures near the critical pressure. However, we prefer to ensure the existence of only single-phase helium in the flow passages. Therefore, flow passages must be sufficiently short to allow high enough flow without pressure loss so great as to drop the fluid pressure below the critical pressure at some point in the windings.

Several alternative flow schemes have been shown to be adequate to remove the projected heat loads to the TF coils of TIBER II.[15] The simplest of these is compatible with a pancake-winding option. Perhaps contrary to intuition, the cold helium in this scheme is injected into the windings at the outermost turns (one inlet at the outer end of each half-pancake). The helium from both halves is exhausted at the same opening on the innermost

and most highly heated turn of the pancake. The exhaust port can be located along the outer leg of the "Dee" where space is available. With the helium injected at relatively low pressures, there is significant JT expansion that gives some added cooling and stablization of temperature in the more highly heated portions of the windings. This can be seen in the path traced out on the TS diagram for the 72 kW total heat load case shown in Fig. 11. The numbers on the curve represent conditions in particular turns of the winding, counting in from the outside.

With temperature distribution in the flow path determined, the conductor is then designed to give the desired performance, i.e. stability margin at the desired J, in the region of the windings where conditions are most severe, i.e. the highest fluid temperature and field. We note here that for the heat loads expected in TIBER II, there are options that hold the fluid temperature in the 12 T region of the TF coils to 5.3 K or less.

PUSHER COIL DESIGN

Conductor optimization--In order to achieve the required average $\dot{i}$ winding pack current density of 40 A/mm^2 in the pusher coil, grading will be necessary. The first grade must operate at 14 T. Subsequent grading steps were chosen for this study at 11 T and 8.5 T, for convenience (an integral number of layers per grade) and for a significant margin of improvement in overall current density beyond the previous, higher-field grade. Figure 12 shows the field distribution through the windings. All conductors have the same generic shape and cable pattern as shown in Fig. 13 but adjustments are made by machine to the external dimensions, the conduit wall thickness, the wire diameter, f_{cond}, and f_{Cu} to satisfy all the requirements of the particular grade and to obtain the highest level of stability permitted by the constraints. All grades are series connected in this design, running at the same current. Table I summarizes important winding pack parameters in the three grades. The fraction of steel was chosen in this iteration to support the electromagnetic hoop loads assuming that each turn should be self supporting. Other parameters were selected by the optimization procedure described above.

-12-

TF COIL DESIGN

The original TIBER TF system^s was designed to produce 10 T with a winding pack current density of 45 A/mm^2. That design also used a MF-Nb$_3$Sn CICC and the cable space current density was about 78 A/mm^2. For TIBER II, 12 T is needed with a winding pack current density of 40 A/mm^2. Protection and structural requirements were the main drivers in the TIBER winding pack design. Those problems will escalate in the larger TIBER II machine. Therefore a larger, more structurally sound variant of the CICC was investigated for the present case. We begin the study with a conductor configuration like that in Fig. 14.

Scaling from the previous TIBER design, it appears possible to achieve J_{pack} = 40 A/mm^2 by setting the cable space current density at about 69 A/mm^2. The current is raised to 35 kA in order that the coil can be protected to the end of machine life with damaged copper (TIBER used a 21 kA conductor).

The important mechanical loads in the critical, central, straight leg region of the winding pack were calculated with EFFI: tension at the midplane is 37.5 MN, maximum pressure due to the centering force is 98 MPa, and maximum pressure due to over turning moments is 39 MPa. These loads are converted to maximum stresses experienced by the structural member of the CICC and indicated in Fig. 14. The tensile stress on the conductor was estimated by assuming only partial load sharing of the tensile loads between the case and the winding pack. The element pictured in Fig. 14 appears at this time to be adequate for use throughout the winding pack, making grading unnecessary, and making the option for pancake winding more reasonable. This is an important point because it makes the option of wind-react-insulate-impregnate more credible. In this technique, the turns of a pancake could be partially spread to accept any choice of turn-turn insulation e.g. the more radiation tolerant polyimides. The proposed winding pack layout and fitup in the central straight section of the case is shown in Fig. 15. Table II summarizes important TF coil and conductor parameters.

TABLE I - Pusher Coil Winding Pack Parameters

	Grade 1	Grade 2	Grade 3
B (T)	14	11	8.5
J (A/mm^2)	66.4	69.0	76.3
f_{cond}	0.73	0.65	0.67
f_{He}	0.27	0.35	0.33
f_{Cu}	0.53	0.66	0.77
f'_{steel}	0.39	0.37	0.36
f'_{insul}	0.08	0.09	0.09
f'_{cond}	0.39	0.35	0.37
f'_{He}	0.14	0.19	0.18
I_{op}/I_c	0.58	0.53	0.55
T_b (K)	4.2	4.2	4.2
T_{cs} (K)	6.4	7.5	8.0
Stab. param.	0.09	0.16	0.14

TABLE II. TF Coil Winding Pack Parameters

Total Current	5.6 MA
Winding-pack cross section	0.140 m^2
Avg. winding-pack, current density	40 $A \cdot mm^{-2}$
Number of turns	160
Conductor current	35 kA
Effective area of a turn (conductor + insulation)	875 mm^2 (33.9 mm x 25.8 mm)
Overall, winding-pack, materials fractions	
f'_{steel}	0.37
$f'_{insulation}$	0.05
f'_{cond}	0.33
f'_{He}	0.25
Conductor, cable-space, cross-section	508 mm^2
Fraction of conductor in the cable-space	0.57
Fraction of copper in the conductor	0.57
Number of cable strands	625 (5^4)
Strand diameter	0.77 mm
Coil dump voltage	10 kV (62.5 V turn-turn)
Est. maximum hot spot temperature	130 K
Est. maximum quench pressure	30 MPa

A_{bz} =   Total cross section of bronze in the CICC (m^2)

A_{Cu} =   Total cross section of copper stabilizer in the CICC (m^2).

A_{fil} =   Total cross section of Nb_3Sn filaments in the CICC (m^2).

A_{sh} =   Total cross section of sheath material in the CICC (m^2).

B   =   Magnetic field at the conductor (T).

$B_{c2m}(0)$ =   Strain-free upper critical field at zero temperature (T).

C_{core} =   Specific heat of noncopper fraction of the composite superconductor. For MF-Nb_3Sn, this amounts to an average of the specific heats of $CuSn$ bronze and Nb_3Sn ($J \cdot kg^{-1} \cdot K^{-1}$).

C_{Cu} =   Specific heat of copper ($J \cdot kg^{-1} \cdot K^{-1}$).

$C_{v,He}$ =   Mean specific heat at constant volume for He, taken as 3100 $J \cdot kg^{-1} \cdot K^{-1}$.

D   =   Damage to the copper stabilizer of a conductor during operation (dpa).

d_W =   Diameter of a superconductor composite strand in the CICC (m).

E_{fil} =   Young's modulus of a Nb_3Sn filament (Pa).

E_s =   Stored energy at full field (J).

E_{sh} =   Young's modulus of the CICC sheath (Pa).

e_p =   The energy density per unit volume of conductor, that can be absorbed by a CICC without quench ($J \cdot m^{-3}$)

$f_{cc \cdot i}$ =   Fraction of conductor inside the conduit of the CICC.

f_{Cu} =   Fraction of stabilizing copper in the superconductor composite strands.

f_{He} =   Fraction of helium inside the conduit of the CICC, $f_{He} = 1 - f_{cond}$.

f_{ret} =   Fraction of damage resistivity retained by the copper stabilizer of a conductor after a room temperature anneal.

i   =   Rate of increase of resistivity returned by the copper stabilizer of a conductor after a room temperature anneal ($n\Omega \cdot m \cdot dpa^{-1}$).

I_c = Critical current at operating field and temperature (A).

I_{cm} = Maximum I_c vs strain (A).

I_{op} = Operating current at full field (A).

I_1, I_2, I_3 = Integral terms defined in text ($A^2 \cdot s^{-1} \cdot m^{-4}$).

J = Operating current density inside the conduit of a CICC ($A \cdot m^{-2}$).

$J_{c0}(B,\varepsilon)$ = Zero temperature critical current density over the noncopper fraction of a composite superconductor strand at field and strain ($A \cdot m^{-2}$).

J_{c0m} = Maximum of J_{c0} vs strain ($A \cdot m^{-2}$).

L = Length of CICC between helium flow connections (m).

ℓ_H = Length of CICC receiving a sudden heat impulse (m).

p_{max} = Maximum allowable, absolute pressure during a quench of the CICC (Pa).

T_b = Bulk fluid temperature of the internal helium of a CICC at operating conditions (K).

$T_c(B,\varepsilon)$ = Critical temperature of the superconductor composite at a particular field and strain (K).

T_{cm} = Maximum of T_c vs strain (K).

V_D = Terminal voltage resulting from a dump at full field (V).

$\left(\frac{\Delta \ell}{\ell}\right)_{fil}$ = Total relative thermal contraction of the Nb_3Sn filament from the conductor heat treatment temperature to operating temperature (i.e. from 1000 K to 4 K).

$\left(\frac{\Delta \ell}{\ell}\right)_{sh}$ = Total relative thermal contraction of the sheath from the conductor heat treatment temperature to operating temperature (i.e. from 1000 K to 4 K).

ε = Total axial strain in the superconductor filaments due to all effects.

$\varepsilon_{init.}$ = Initial axial strain in the superconducting filaments after cooldown to operating temperature.

ε_{sh} = Axial strain added to the sheath of the CICC under the action of electromagnetic forces.

η = Stability parameter.

$\mu_{He,init.}$ = Density of the internal He in a CICC at the initial operating temperature and pressure (i.e. before a quench) ($kg \cdot m^{-3}$).

μ_{core} = Density of the noncopper fraction of the composite superconductor (taken as 8920 $kg \cdot m^{-3}$ for MF-Nb_3Sn composites).

μ_{Cu} = Density of copper (taken as 8940 $kg \cdot m^{-3}$).

$\rho_{Cu}(B)$ = Resistivity of the stabilizing copper at operating field ($\Omega \cdot m$).

ρ_d = Resistivity added to the residual value by radiation damage ($\Omega \cdot m$)

ρ_s = Saturation value of stabilizer residual resistivity due to radiation damage ($\Omega \cdot m$).

ρ_o = Residual resistivity ($\Omega \cdot m$). A subscript i indicates initial, undamaged value.

$\sigma_{Cu,y}$ = Yield stress of copper (Pa).

$\sigma_{bz,y}$ = Yield stress of bronze (Pa).

τ_H = Duration of a sudden heat impulse to the CICC (s).

τ_R = Recovery time in a CICC from the normal excursion caused by a sudden thermal perturbation (s).

REFERENCES

1. J. W. Lue and J. R. Miller, "Performance of an Internally Cooled Superconducting Solenoid," Adv. Cryog. Eng. 27 227 (1982)

2. J. L. Young et. al., The Force Flow Cooled Coils For the International Energy Agency Large Coil Task," Adv. Cryog. Eng. 27, 11 (1982).

3. M. O. Hoenig et. al., "MIT 12 Tesla Coil Experimental Results," Adv. Cryog. Eng. 31 151 (1986).

4. M. SUENAGA, Brookhaven National Laboratory, Upton, NY, private communication, July 1985.

5. C. D. Henning et. al., "TIBER--Tokamak Ignition/Burn Experimental Research: Final Design Report," LLNL Internal Report Number UCID-20589, November 1, 1985.

6. R. FLUKIGER, W. MAURER, & F. WEISS, Kernforschungszentrum, Karlsruhe, FRG, and P. HAHN and M. GUINAN, Lawrence Livermore National Laboratory, Livermore, CA, presentation at a high-field magnet workshop in Karlsruhe, FRG, March 1986.

7. Various formulae constructed to fit data presented in: M. W. Guinan, "Radiation Effects Limits on Copper in Superconducting Magnets," LLNL Internal Report Number UCID-19800, May 25, 1983.

8. J.R. MILLER et al., "The Initial Filament Strain State of Cable-in-Conduit Superconductors and The Relation of this Strain to Large-Bore, High-Field Magnet Design," presented at the Applied Superconductivity Conference, Baltimore, MD, September 28 – October 3, 1986.

9. M.M. STEEVES et al., "Effects of Incoloy 903 and Tantalum Conduits on Critical Current in Nb_3Sn Cable-in-Conduit Conductors," Adv. Cryog. Eng. 30, 883 (1982).

10. R.M. SCANLAN et al., "Mechanical Properties of High-Current Multifilamentary Nb_3Sn Conductors," Filamentary A15 Superconductors, M. Suenga and A.F. Clark, Eds. (Plenum Press, New York, 1980) p. 221.

11. J.W. EKIN, "Strain Scaling Law for Flux Pinning in Practical Superconductors. Part 1: Basic Relationship and Application to Nb_3Sn Conductors," Cryogenics 20, 611 (1980).

12. J.R. Miller et al., "High Field Superconducting Magnets (12 T and Greater) for Fusion Applications," presented at the Seventh Topical Meeting on The Technology of Fusion Energy, Reno, Nevada, June 15-19, 1986 and references cited therein.

13. R. D. McCarty, "Thermodynamic Properties of Helium 4 from 2 to 1500 K at pressures to 10^8 Pa," <u>Journal of Physical and Chemical Reference Data</u> <u>2</u> 923 (1973).

14. L. DRESNER, "The Growth of Normal Zones in Cable-in-Conduit Superconductors," <u>10th Symposium on Fusion Engineering Proceedings</u> (IEEE Cat. No. 83CH1916-6 NPS, IEEE Service Center, Piscataway, NJ, 1983), Vol. 2, p. 2040.

15. C.D. Henning and B. G. Logan, eds. "TIBER II, Tokamak Ignition/Burn Experimental Reactor 1986 Status Report," LLNL internal report UCID-20683, October 23, 1986.

ms609049R
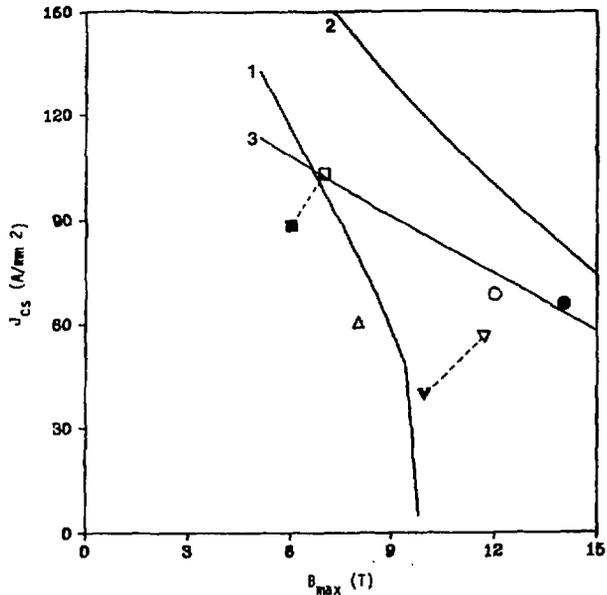
Figure 1. Experience and obtainable performance in terms of cable space current/density vs. field with coils using cable-in-conduit conductors:

■ operation of the ORNL, NbTi solenoid[1] with measured stability in excess of 100 mJ·cm^{-3}; □ operation of the ORNL NbTi solenoid[1] with measured stability over 50 mJ·cm^{-3}; Δ planned operation of the Westinghouse, MF-Nb$_3$Sn LCT coil[2]; ▼ operation of the MIT 12T coil (MF-Nb$_3$Sn) at high stability (full margin unmeasured because of failure of pulsed heaters)[3]; ∇ stable operation of the MIT 12 T coil into the current sharing regime[3]; o design goal for the TIBER II TF coils; ● design goal for the high field grade of the TIBER II central plasma shaping coil; Curve 1 – estimate of obtainable performance with a cable-in-conduit conductor using presently available NbTi; Curve 2 – estimate of obtainable performance with a cable-in-conduit conductor using presently available MF-Nb$_3$Sn; and Curve 3 – estimate of performance for the same conductor as Curve 2 but with an accounting for reduced stability margin due to degradation of copper stabilizer conductivity at the level of radiation exposure expected in TIBER II.
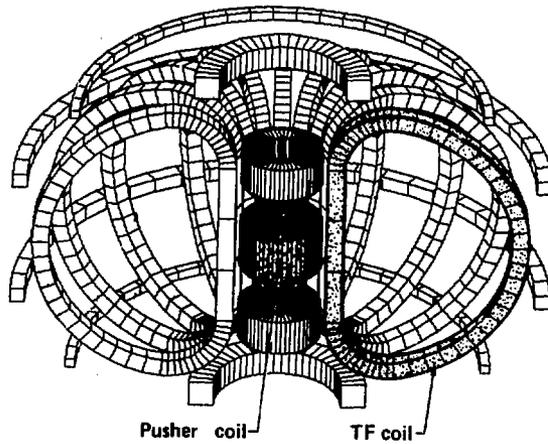
Figure 2.   The TIBER II magnet system.
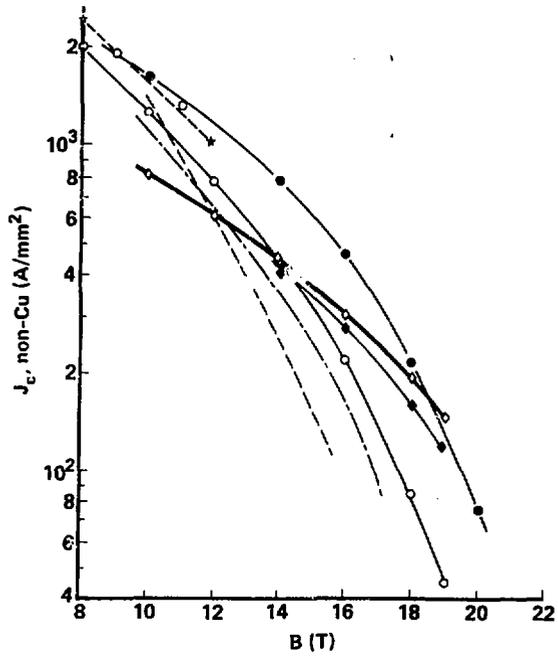
Figure 3. Recent critical current data for various MF-Nb$_3$Sn conductors at 4.2 K. Solid Curves represent (NbTi)$_3$Sn and broken curves represent "pure" MF-Nb$_3$Sn variations.
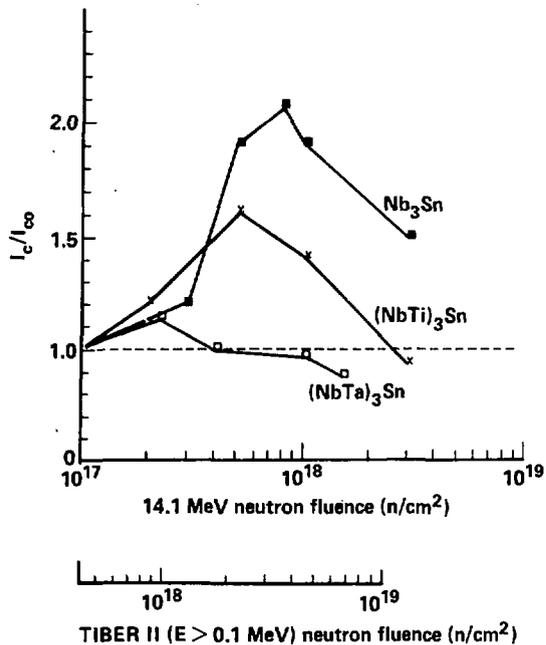
Figure 4. Critical current vs neutron fluence. Data were taken using a 14.1-MeV neutron source. The lower horizontal axis accounts for the "softer" neutron energy spectrum expected in TIBER-II.
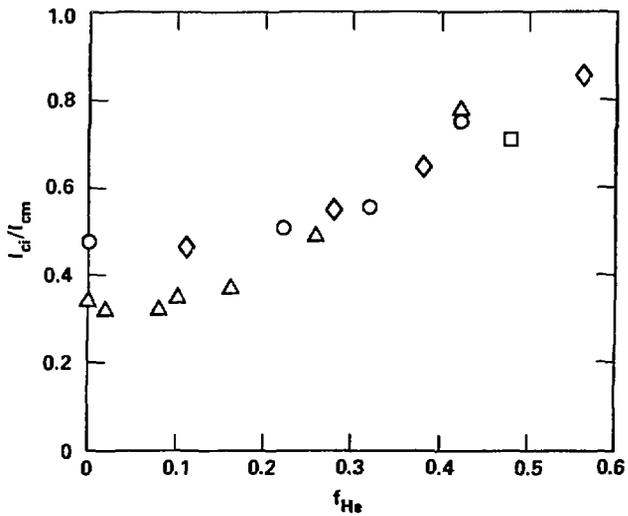
Figure 5. Ratio of initial (unloaded) critical current of CICC samples to maximum critical current as a function of void or helium fraction inside the conduit.
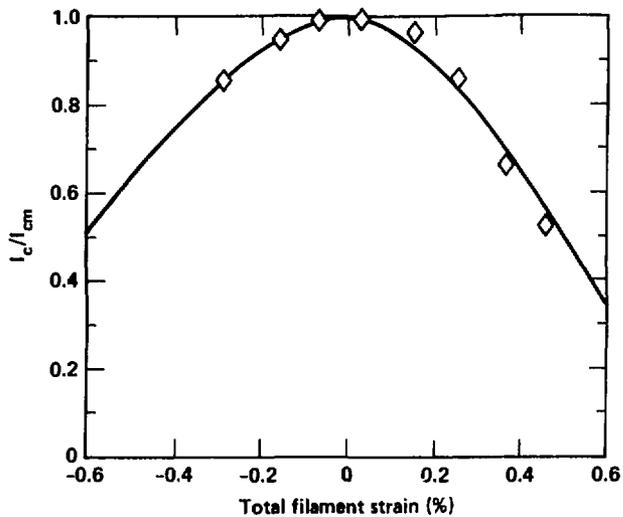
Figure 6. The effect of strain on critical current of a bronze-processed
MF-Nb$_3$Sn conductor at 12 T, 4.2 K. The curve fitted to the data
uses Ekin's formalism with $B_{c2m}(0) = 22$ T and $T_{c0m} = 18$ K.
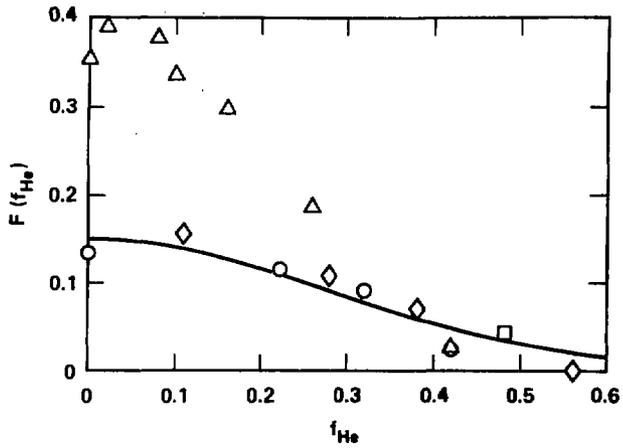
Figure 7.   Data of Fig. 5 converted to values of $F(f_{He})$ using Eq. 1 and I_c/I_{cm} as a measure of filament strain, as given in Fig 6.
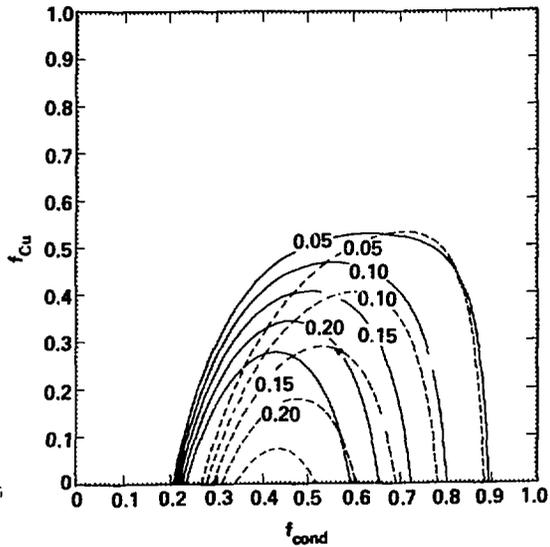
Figure 8. An illustrative example of contours of η in the (f_{cond}, f_{Cu}) plane for particular J, B and T values. Dashed contours ignore conductor strain effects. Solid contours account for strain as discussed in the text.
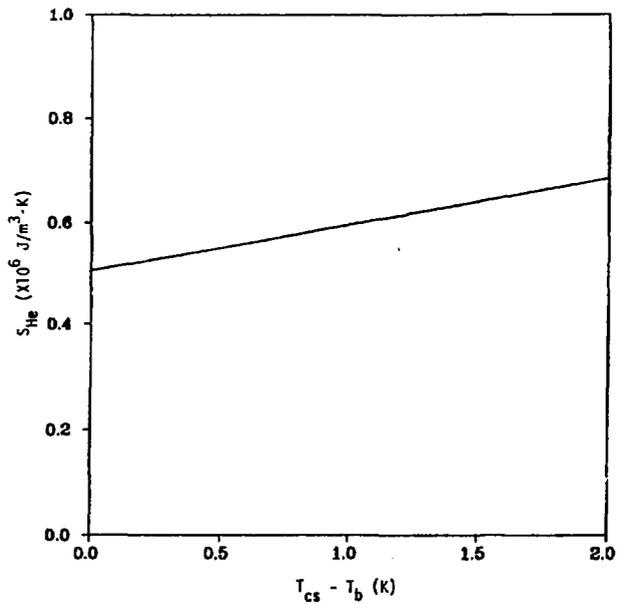
Figure 9. Effective mean volumetric heat capacity of the helium internal to a CICC between the initial bulk fluid temperature T_b and the current sharing temperature T_{cs} vs the difference $T_{cs} - T_b$
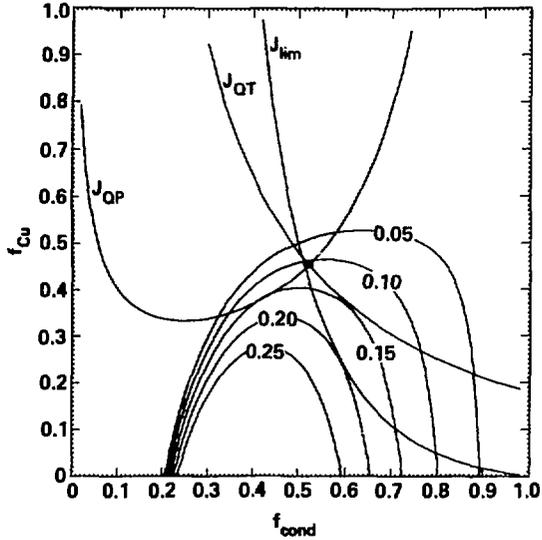
Figure 10. Typical contours of η in the (f_{cond}, f_{Cu}) plane with fixed J in a particular design, B and T. Boundary curves embodying the constraints on J as discussed in the text define acceptable values of f_{cond} and f_{cu}: the curve labeled J_{lim} represents the constraint in (3), J_{QT} represents the constraint in (5), and J_{QP} represents the constraint in (6). The allowed values are those that lie on or above all of these curves. Therefore, the configuration simultaneously satisfying the constraints and providing the highest stability for this particular J, B and T represented by the dot.
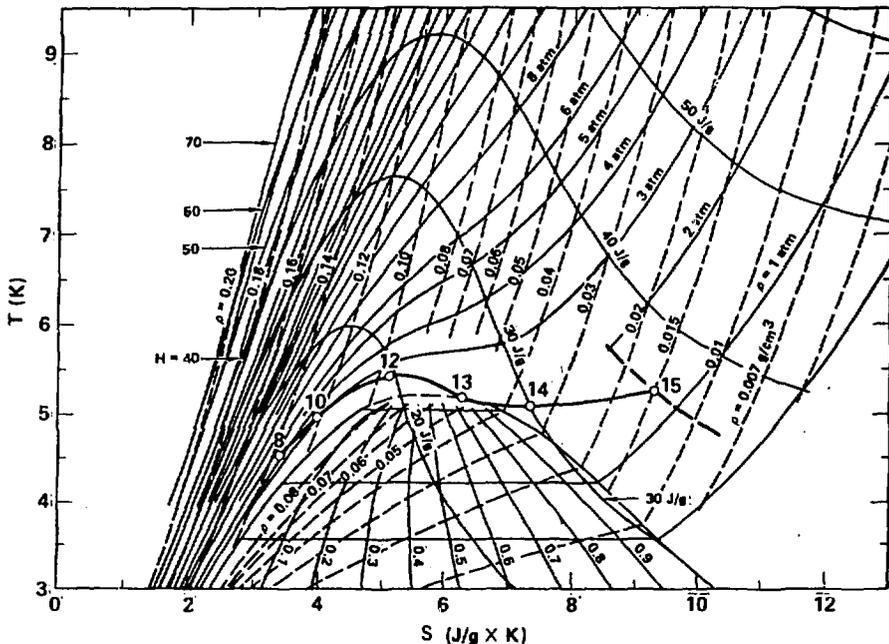
Figure 11. Thermodynamic path taken by the helium in a TIBER II TF coil corresponding to a total radiation heat load of to all coils 72 kW. The numbers on the curve are turn numbers, helium is injected at the outside (Turn 1) at 4.5 K, 5 atm, and flows toward the inside. In the first eight turns heating is negligible. After that the temperature rises somewhat due to a combination of heating and expansion. Then cooling due to JT expansion in the inner turns essentially matches radiation heating to hold the temperature nearly constant. Total helium flow for this case is 3000 g.s^{-1}.
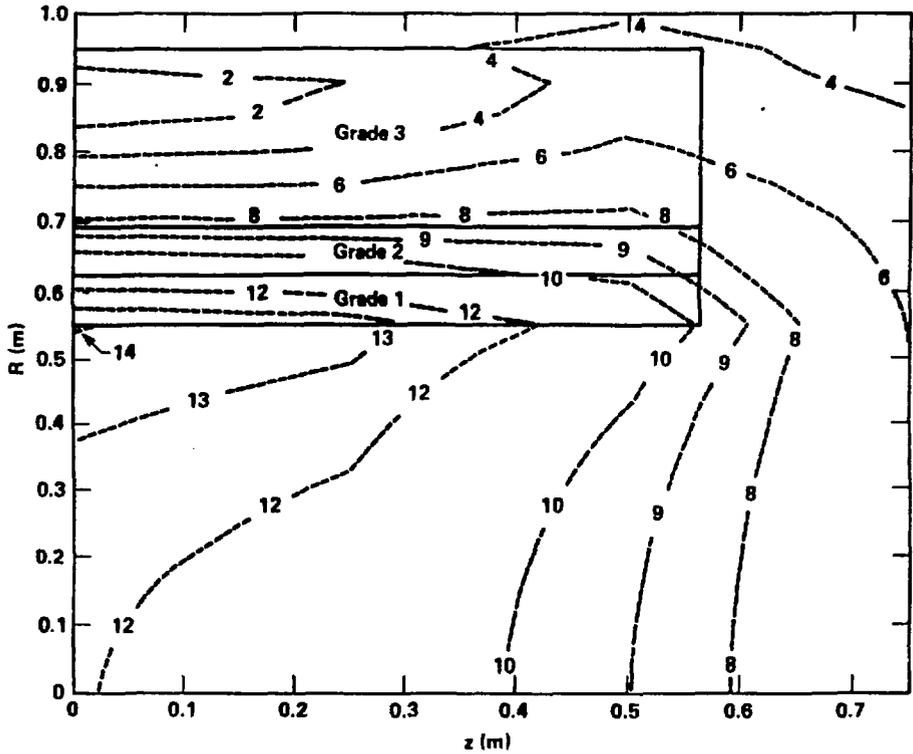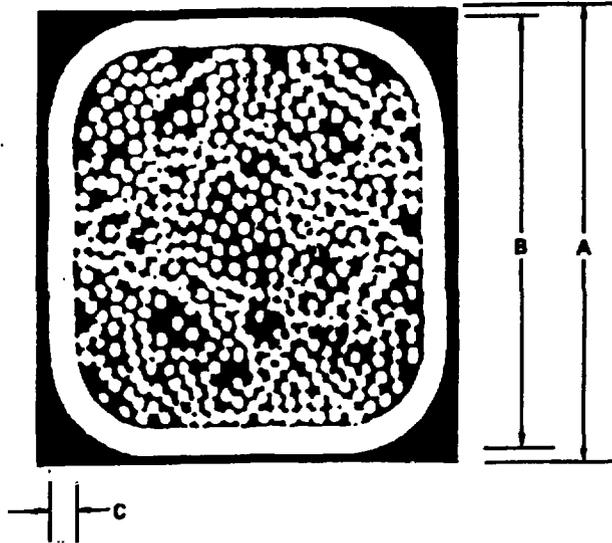
Figure 12. Cross section of the upper half of the pusher coil showing field contours and the selection of grading steps.

	B_{max}	I	J_{pack}	A	B	C
	(T)	(Amps)	(A/mm^2)	(mm)	(mm)	(mm)
Grade 1	14	20,000	35.0	23.9	22.9	2.77
Grade 2	11	20,000	37.5	23.1	22.1	2.53
Grade 3	8.5	20,000	42.1	21.8	20.8	2.31

$$\langle J_{pack} \rangle = 40 \ A/mm^2$$

Figure 13. General configuration and dimensions of the conductors plus insulation used in the three grades of the pusher coil windings.
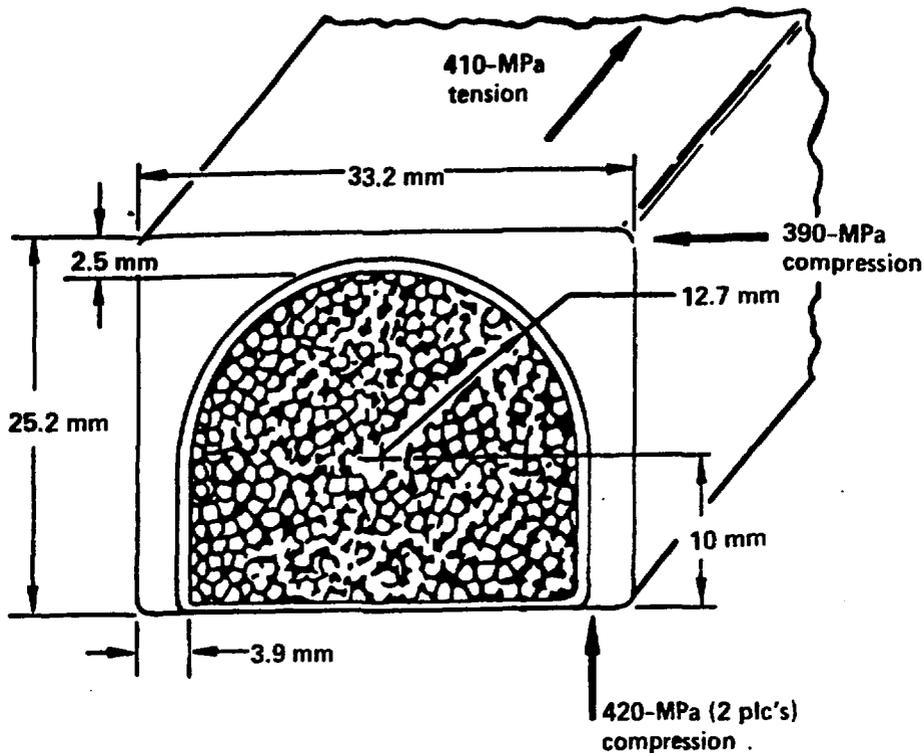
Figure 14. Proposed TIBER II TF conductor with indications of the maximum
stresses in the channel due to tension, centering, and
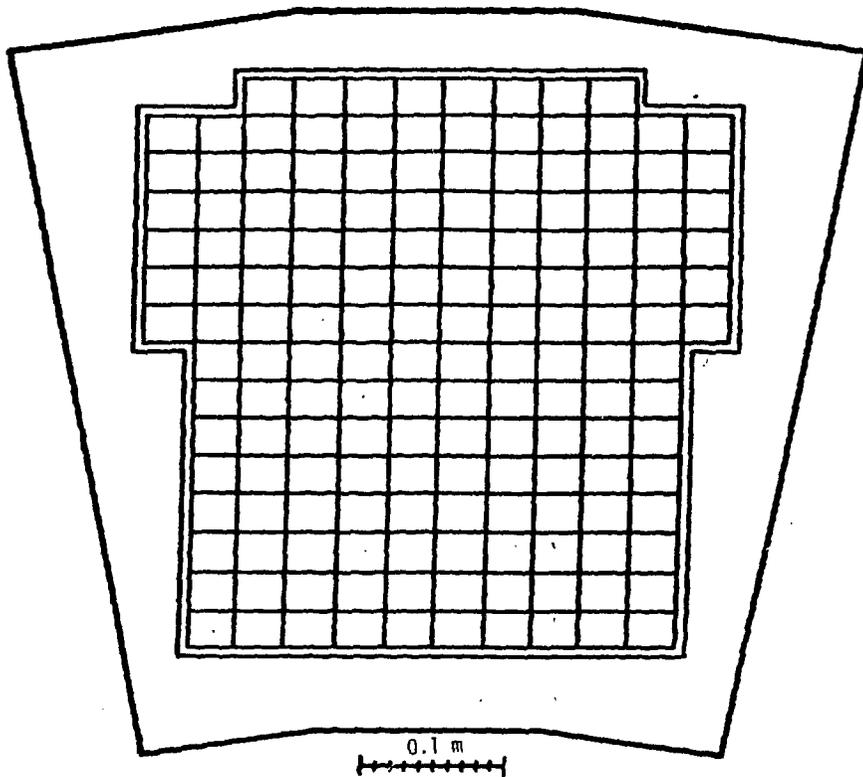overturning loads in the central, "straight leg" region of the
TF coil.

0.1 m

Figure 15. TF coil section.